Chapter 14
Picosecond Magnetization Dynamics of Nanostructures Imaged with Pump–Probe Techniques in the Visible and Soft X-Ray Spectral Range

Philipp Wessels and Markus Drescher

Abstract The most direct way of accessing and understanding fast dynamical processes in nature is by capturing the motion in real space with a high temporal and spatial resolution. This chapter details time-resolved imaging techniques for probing the transient evolution of the magnetization in small magnetic systems in the visible and soft X-ray spectral range. Optical methods using femtosecond laser pulses can follow ultrafast processes with an extreme temporal resolution. The spatial resolution, however, is limited by diffraction to a few hundred nanometers at visible wavelengths. The dynamics of smaller structures can be investigated using X-ray microscopy at synchrotron radiation sources. A resolution of a few ten nanometers can be achieved, however, the time-resolution is limited to a few hundred picoseconds due to the pulse duration of the synchrotron bunches. Spin-wave packets are captured by optical methods using a time-resolved confocal Kerr microscope where backward volume spin-wave packets with counterpropagating group- and phase velocity are observed directly. Time-resolved X-ray microscopy is used to monitor the destruction and emergence of equilibrium domain patterns out of uniformly magnetized states.

Magnetic systems have proven to be very efficient data storage elements so that nowadays the majority of information is recorded on magnetic hard-disk-drives. Information can be encoded in a persistent way by aligning the magnetization of ferromagnetic elements. In order to achieve a high data-density, the size of these magnetic bits has to decrease and has approached domain sizes around 20 nm at 1 Tbit/in^2 data densities in commercially available hard disks. The nature of magnetism in such nanoscale systems has to be understood very well in order to further diminish the domain size and the spacing between adjacent bits. Ideally, a direct

P. Wessels · M. Drescher (✉)
The Hamburg Centre for Ultrafast Imaging (CUI), Hamburg, Germany
e-mail: markus.drescher@physik.uni-hamburg.de

P. Wessels
e-mail: pwessels@physnet.uni-hamburg.de

M. Drescher
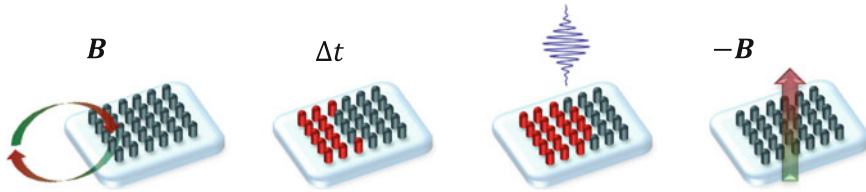Institut Für Experimentalphysik, University of Hamburg, Hamburg, Germany

Fig. 14.1 Pump–probe/reset sequence for studying magnetization dynamics: A magnetic sample can be excited via a local magnetic field pulse $\boldsymbol{B}$ so that the magnetization evolves in time. Here, single-domain elements in a nanomagnetic array start reversing their magnetization (*red dots*). A snapshot of the magnetization pattern after a certain time Δt can be imaged by a light pulse. If the dynamic process is non-reversible, the magnetization has to be reset by a global field pulse $-\boldsymbol{B}$. Repetition of this process for a varying time delay Δt leads to a movie sequence of reproducible events. Adapted from P. Wessels, Ph.D. thesis (Verlag Dr. Hut, München, 2014) [1]

real-space observation is favored to investigate magnetic systems at such small length scales.

Magnetism, moreover, is no static phenomenon and domains in a magnetic system can reorganize and evolve in time. Adjacent magnetic elements, for example, may see the stray-field of neighboring elements and trigger dynamics that might delete stored information when decreasing the bit distance in storage media. A locally excited coupled spin-system will transfer such an excitation due to interactions so that spin-waves emerge. These dynamic processes occurring in micro- and nanoscale elements evolve on very fast time-scales in the nano- to femtosecond range so that an instrument capable of following magnetization dynamics in these elements does not only need a high spatial but also a high temporal resolution.

This can be achieved with ultrashort light pulses providing extremely fast imaging flashes for the observation of magnetization dynamics by employing the pump–probe technique introduced in Fig. 14.1. A sample is excited by a short magnetic field pulse and a snapshot of the magnetization is captured by a laser pulse after a variable time Δt. By repeating this procedure for several time delays Δt, a movie of the reproducible dynamics can be reconstructed. However, structures below 200 nm size can not be resolved with visible light due to the fundamental diffraction limit at optical wavelengths. The use of soft X-ray radiation available for example at synchrotron radiation sources extends the observable structural size down to a few nanometers where the resolution is limited by the fabrication capabilities of X-ray optics. However, the time-resolution usually is not competitive with laser-based instruments since the light pulses in a storage ring are typically a few hundred picoseconds long so that faster processes can not be followed.

In Sect. 14.1 we present how magnetization dynamics can be explored in real-space and real-time using optical techniques with a high temporal but a medium spatial resolution where the investigation is focused on spin-wave packets in magnetic micro-stripes. An opto-electronic high peak-current source enables the excitation and direct observation of backward volume spin-wave packets in permalloy ($Ni_{80}Fe_{20}$). These modes feature the unusual property of a negative group velocity where the phase fronts move in the opposite direction of the propagating wave packet.

Soft X-ray microscopy discussed in Sect. 14.2, allows for imaging with a higher spatial but a lower temporal resolution so that magnetization processes in nano- and microstructures can be followed where domain pattern destruction and recovery has been observed. For this purpose a full-field imaging X-ray microscope has been set up at the 3rd generation synchrotron source PETRA III that is equipped with a gated detector so that time-resolved pump–probe experiments can be performed. Here, an intense magnetic field pulse saturates the magnetization of a permalloy microsquare and subsequently the build-up of the equilibrium domain pattern can be followed by the X-ray microscope. This allows direct access to the domain formation process and sheds light on the question how (fast) magnetic domains form.

Recent experiments have shown alternative approaches for time-resolved imaging of small magnetic samples. For example an investigation of spin-wave solitons has been performed using X-ray microscopy [2]. Another experiment has demonstrated the time-resolved capabilities of scanning electron microscopes with polarization analysis [3].

14.1 Direct Observation of Spin-Wave Packets in Permalloy

Besides the routine use of ferromagnetic elements in data storage, magnetic structures also have the potential to solve a problem of increasing importance when building smaller and faster miniaturized circuits: In conventional electronic devices information is transported and processed by moving electrons steered by their electric charge. This involves friction so that heat is generated which limits the clock rate in such circuits, especially in mobile devices where active cooling is not an option.

Instead of using the charge for information transport and processing also the magnetic moment - or spin - of electrons can be utilized to complete these tasks. The advantage of magnetic transport is the negligible heat load since particle movement is not necessary because the information is transferred purely by interactions of neighboring spins. The research field of spintronics [4–6] is dedicated to building magnetic devices for signal transport and processing which may extend or even replace conventional electronic circuits. Magnetic moments can be driven into a precessional motion and the gyration frequency in metallic ferromagnetic structures such as permalloy ($Ni_{80}Fe_{20}$) is compatible with current clock rates of several GHz in conventional electronic microprocessors. This motion can be transferred in confined magnetic structures so that spin-waves emerge (compare also Fig. 14.3a). The wavelength of spin-waves in permalloy is in the μm to nm range also matching the size of logical units in conventional electronics.

Extensive research has been carried out to study the properties of spin-waves and their application to logic devices [7–9]. Most experiments focus on continuously excited spin-waves but to implement a scheme for encoding information the wave's amplitude or phase has to be modified dynamically. In this work we address spin-wave packets and investigate the dynamical properties such as phase- and group velocities as well as the dispersion of these wave packets.
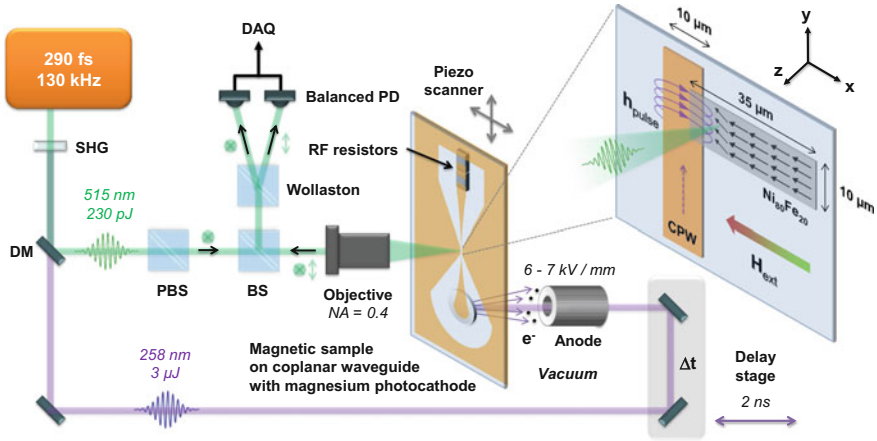
Fig. 14.2 Time-resolved scanning Kerr microscope: Ultrashort visible laser pulses of 290 fs pulse duration are converted into the ultra-violett (UV) spectral range via second harmonic generation (SHG). The delayable UV pulses trigger a magnesium photocathode on a coplanar waveguide (CPW) supplied by a static extraction field. The generated current pulses propagate through the waveguide and are terminated in a series of radio-frequency (RF) resistors. The co-propagating magnetic field h_{pulse} is able to excite spin-wave packets in a permalloy ($Ni_{80}Fe_{20}$) layer in the center of the waveguide. The residual visible light pulses are separated by a dichroic mirror (DM), poralization filtered by a polarizing beamsplitter (PBS) and focused onto the magnetic sample. The polarization change due to the magneto-optical Kerr effect (MOKE) is analyzed behind an intensity beamsplitter (BS) and Wollaston prism in a balanced photodetector (PD). This observable is proportional to the z component of the magnetization. By scanning the sample through the laser focus and variation of the pump–probe delay Δt, a movie of the spin-wave packets can be captured. Adapted from P. Wessels et al., Sci. Rep. **6**, 22117 (2016) [10]

The experimental setup for exciting and capturing spin-wave packets is presented in Fig. 14.2 and described in more detail in [1, 10]. Briefly, a confocal scanning microscope analyzes the polarization of a laser pulse in the visible spectral range reflected by a magnetic sample. The polarization change after reflection encodes information on the out-of-plane component of the sample magnetization via the magneto-optical Kerr effect (MOKE). Synchronized ultraviolet (UV) laser pulses release electrons via the photoeffect from a metallic photocathode fabricated onto the sample. The emerging current pulse propagates towards the magnetic sample in a tapered coplanar wave-guide (CPW) where the copropagating magnetic field is able to trigger magnetization dynamics in the vicinity of the waveguide conductor. The magnetic moments starts to gyrate around the axis of an external magnetic field and due to interactions a spin-wave packet is launched which propagates along the permalloy microstripe.

Spin-waves in confined magnetic structures can be excited in different configurations. Most popular are Damon-Eshbach (DE) modes where an external bias field is aligned perpendicular to the propagation direction of the spin-wave. These modes are easy to excite and feature high gyration frequencies and small wavelengths in fer-
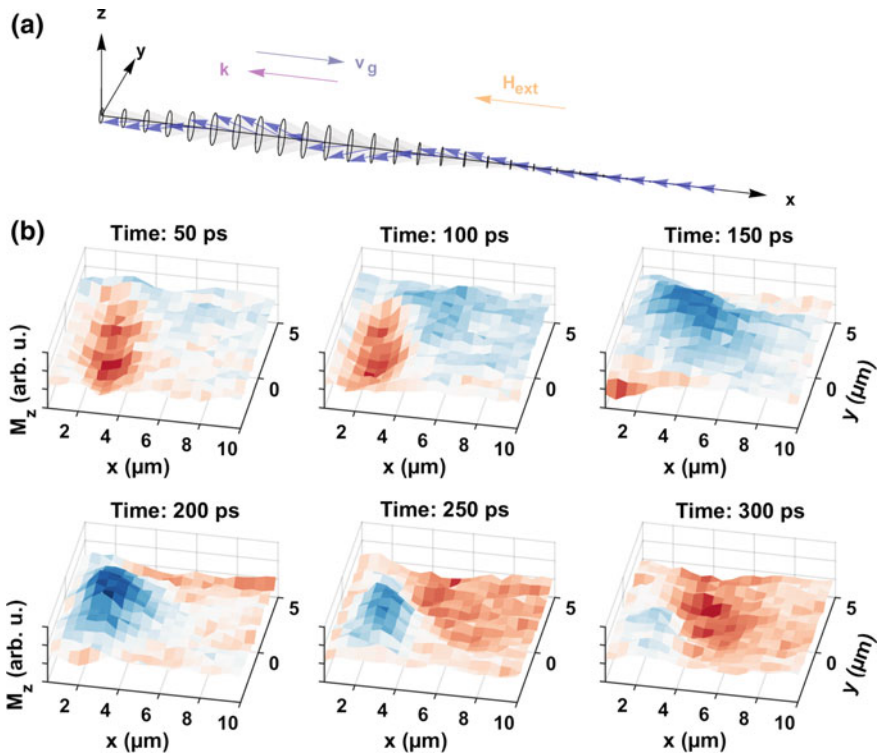
Fig. 14.3 Observation of a backward volume spin-wave packet: **a** Geometry of the precessional motion. An external bias field H_{ext} aligned parallel to the wave vector **k** features backward volume spin-wave packets with a negative group velocity v_g so that the phasefronts propagate into the opposite direction of the wave packet. **b** Snapshots of the magnetization for six delays Δt. The wave packet is excited on the left around $x = 2\,\mu m$ and propagates to the right along the positive x axis. The phase-fronts clearly approach the source region from the right side indicating that phase- and group velocity are counteraligned. Reproduced from P. Wessels et al., Sci. Rep. **6**, 22117 (2016) [10]

romagnetic layers. Thus, experimental efforts have focused on continuously excited DE spin-waves via a radio-frequency (rf) current coupled into a waveguide. For information processing, however, an impulsive excitation is favorable so that information encoded into spin-wave bursts can be transported and processed. Damon-Eshbach spin-wave packets are directional, meaning that a certain propagation direction is favored. Similar to most coupled systems the oscillating phase-fronts propagate into the same direction as the wave packet envelope so that wave vector **k** and group velocity v_g point into the same direction. For detailed studies of directly captured DE spin-wave packets in permalloy microstripes with the time-resolved MOKE microscope the reader is referred to [10].

By changing the direction of the bias field parallel to the propagation direction of the phase-fronts (compare Fig. 14.3a), another mode called backward volume (BV)

mode is favored which is usually harder to excite compared to DE spin-waves [11]. We have captured and analyzed such BV modes in ferromagnetic metallic permalloy layers by making use of a high peak current source in form of a metallic photocathode. The results are presented in Fig. 14.3b. Characteristic for such modes is a phase front motion that is counteraligned to the propagation direction of the wave packet. While the wave packet is excited on the left side of the frame, new phase fronts emerge from the right side approaching the source region as time elapses. The precession frequency of the wave packet is 3.5 GHz and more details are discussed in [10]. BV spin-wave packets have been observed in ferrimagnetic insulators [12], however, an excitation in metallic ferromagnets such as permalloy features a considerable lower damping and smaller wavelength where micro- [13–15] and nanoscale [2, 16, 17] excitations have been reported which is favorable for the development of logic devices. Usually, BV spin-wave packets are experimentally observed in ferrimagnetic yttrium iron garnet $Y_3Fe_5O_{12}$ (YIG) which benefits from a low damping constant but the wavelength typically lies in the mm range and the fabrication of the monocrystalline layers is demanding.

Spin-wave packets not only implement a data transport and processing protocol with negligible heat load. The unusual dispersion relation of BV modes where the group velocity is negative and the phase front motion counteraligned to the propagation direction serves as a simulator toolkit for electromagnetic waves in negative refractive index media such as metamaterials. A negative refractive index ($n < 1$) is equivalent to a negative scalar product of phase- and group velocity ($v_{ph} \times v_g < 1$). Often only simulations provide access to the phase-resolved electromagnetic field in such materials. A sample with an engineered BV dispersion relation can serve as a model system for studying more complex spin-wave dynamics such as interference, reflection etc. for designing advanced metamaterials.

14.2   Time-Resolved Imaging of Domain Pattern Destruction and Recovery

Soft X-ray radiation as delivered by synchrotron radiation sources is a well suited tool for magnetic imaging. The short wavelength enables a high spatial resolution and via the X-ray magnetic circular dichroism (XMCD) the magnetization of a sample can be mapped with element specificity. Due to the pulsed character of synchrotron radiation also time-resolved experiments can be performed so that magnetization dynamics can be captured with a typical time resolution of about 100 ps.

X-ray microscopy has provided tremendous insight into magnetic nanostructures and their dynamics [18, 19]. Due to the high absorption of soft X-ray radiation in almost all materials the use of conventional refractive optics in such microscopes is not possible. Instead, one relies on holographic techniques or refractive optics such as zone plates where the outermost zone width determines the achievable resolution. Usually, these endstations operate as transmission microscopes where a thin sample
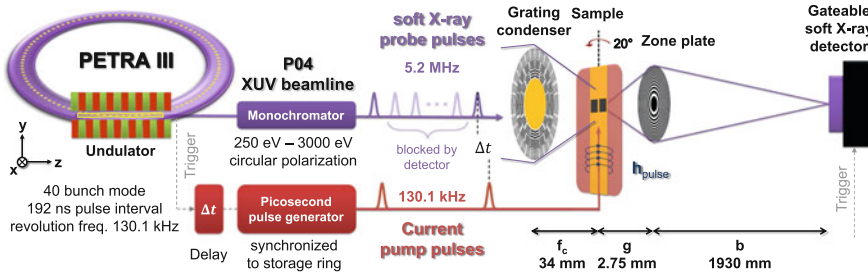
Fig. 14.4 Magnetic full-field X-ray microscope with time-resolution: Soft X-ray flashes generated by the storage ring PETRA III are monochromatized in the P04 beamline and focused onto a magnetic sample located on the conductor of a coplanar waveguide (CPW) by a grating condenser. The transmitted light is imaged by a zone plate onto a gateable detector. Magnetization dynamics can be triggered by injecting picosecond current pulses into the waveguide where the copropagating magnetic field h_{pulse} excites the sample. The dynamics can be followed by taking snapshots for several delays Δt between pump and probe pulse. Adapted with permission from P. Wessels et al., Phys. Rev. B **90**, 184417 (2014) [23]. Copyrighted by the American Physical Society

layer is deposited onto a silicon nitride membrane with a high transmission for soft X-ray radiation. For time-resolved measurements most instruments are operated in scanning mode where the X-rays are focused onto the sample by a zone plate and the transmitted radiation is detected by a fast photodiode. We have demonstrated the first realization of a full-field X-ray microscope with time-resolution where the sample is illuminated by a condenser zone plate and imaged by a micro zone plate onto a gated two–dimensional detector [20–23].

The experimental setup is depicted in Fig. 14.4. In contrast to many other X-ray microscopes, the developed instrument is not a fixed endstation but a mobile unit that can be installed for example at the 3rd generation synchrotron radiation source PETRA III at DESY in Hamburg. The soft X-ray undulator beamline P04 [24] delivers monochromatized circularly polarized photons in the energy range of 250–3000 eV. In time-resolved mode the storage ring is filled with 40 bunches circulating at a repetition rate of 130.1 kHz.

The synchrotron light is collected by a grating condenser [25] that creates a homogeneously illuminated spot on the magnetic sample. The transmitted light is imaged onto a two–dimensional detector by a micro zone plate with an outermost zone width of 50 nm so that the spatial resolution is limited to 65 nm according to the Rayleigh criterion.

The magnetic sample is excited by intense current pulses at a repetition rate of 130.1 kHz synchronized to the storage ring round trip frequency. The pulses are injected into a tapered coplanar waveguide and the copropagating magnetic field h_{pulse} is able to initiate magnetization dynamics in the sample located on the conductor of the waveguide. The sample is tilted by 20° to be sensitive to in-plane magnetization components.

The full-field microscope directly images the sample plane onto a two–dimensional detector. For time-resolved studies a single out of 40 bunches of the storage ring has
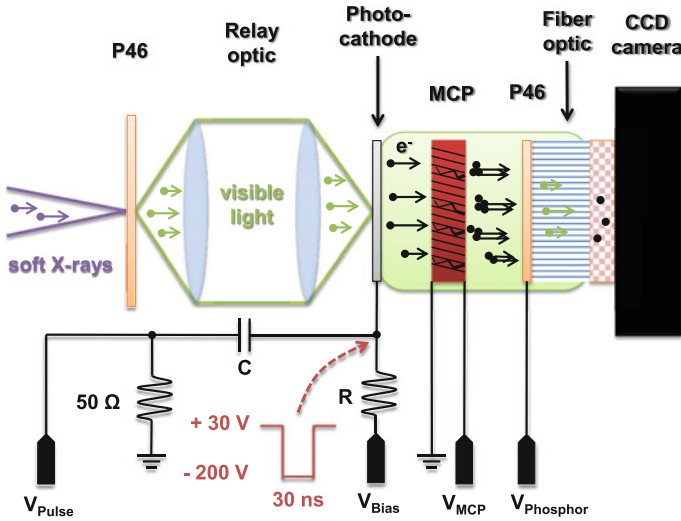
Fig. 14.5 Gateable two–dimensional X-ray detector: The sample image is projected onto a P46 phosphor screen and the emitted visible light transferred via a relay optic onto the photocathode of an image intensifier assembly. By applying a negative voltage pulse to the photocathode the emitted electrons are passed onto a microchannel plane (MCP) where the signal is amplified and converted into visible light by another P46 phosphor screen fiber-tapered onto a CCD camera. To block light from a bunch, a positive bias voltage is applied to the photocathode so that the electrons can not reach the MCP. Reproduced from J. Ewald et al., AIP Conf. Proc. **1696**, 020005 (2016) [22], with the permission of AIP Publishing

to be isolated. Available cameras cannot continuously be read out at the necessary 130 kHz rate, so that a gating technique has to be applied. Figure 14.5 depicts the layout of the gateable X-ray detector. The micro zone plate projects the sample plane onto a P46 phosphor screen mounted on a window inside the vacuum chamber. The emitted visible light pulse is transferred by two fast camera lenses in a relay configuration onto the photocathode of a commercial image intensifier. The photocathode is biased with a positive voltage so that the electrons by default can not escape the cathode surface. By applying a short negative gate pulse of 30 ns and -200 V amplitude the electrons are passed on to the front side of a microchannel plate (MCP) where the signal is amplified and accelerated onto another P46 phosphor screen that converts the electronic signal into visible light. The output port of the phosphor screen is fiber-tapered onto the CCD chip of a cooled camera where the image is recorded.

Due to the intense excitation pulse, the sample can only be excited at the round trip frequency of the storage ring of 130.1 kHz while the ring is filled with 40 bunches. This means that only one bunch contains a dynamic signal so that images generated by the remaining 39 bunches have to be filtered out by the gateable detector. The gate pulse duration of 30 ns and the decay time of the P46 phosphor screens ($\approx$200 ns) are fast enough to isolate light from single bunches in the detector (compare also [1, 21, 22]). For a fixed delay Δt the signal can be integrated on the camera chip until a sufficient signal-to-noise ratio has been reached.
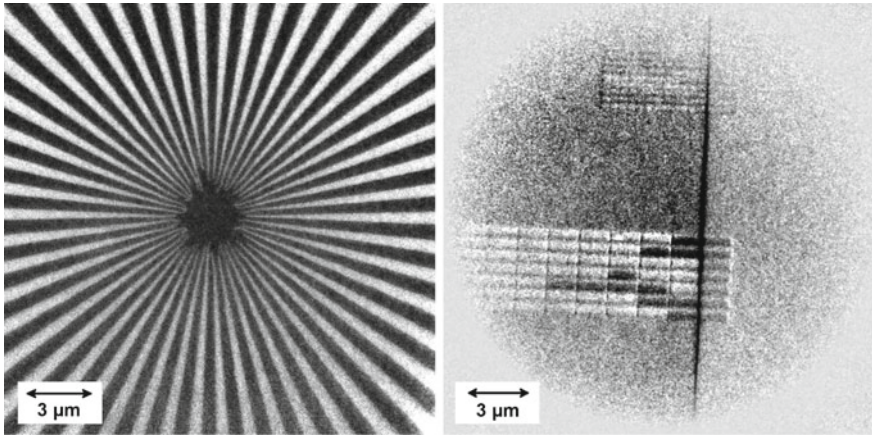
Fig. 14.6 Siemens star and array of magnetic elements: The Siemens star with 50 spokes is imaged at a magnification of $M = 700$. The central part of the XMCD image on the right shows the magnetization configuration of an array of $1.3 \times 0.3 \,\mu\text{m}^2$ permalloy elements of 10 nm thickness separated by $\approx$40 nm. The magnetization of some elements points to the right side of the image (dark contrast) while other elements are aligned to the left side (white contrast). Adapted from P. Wessels, Ph.D. thesis (Verlag Dr. Hut, München, 2014) [1]

To demonstrate the imaging capabilities of the X-ray microscope, a Siemens star with 50 spokes is recorded at a magnification of $M = 700$ in Fig. 14.6 on the left. The Siemens star supports a resolution where features below 75 nm are discernible. The inner part of the Siemens star is obscured by lithography remnants so that no statement on a possibly higher resolution can be made here.

The (static) magnetic imaging capabilities are demonstrated on the right image in Fig. 14.6. An array of $1.3 \times 0.3 \,\mu\text{m}^2$ permalloy elements of 10 nm thickness separated by 40 nm are presented here. The separation is still resolvable with the X-ray microscope. For XMCD measurements, the instrument is operated at the nickel L_3 edge at a photon energy of 852.7 eV with a bandpass of 1 eV. An XMCD image is obtained by capturing two images with circular polarized light at opposite photon helicities. The helicitiy can be changed from σ^+ to σ^- by shifting the magnetic structures in the beamline undulator. The difference of the two images directly maps the magnetic orientation in the sample. Elements aligned homogeneously along the x axis (dark contrast) as well as elements aligned into the opposite direction (white contrast) are visible. Dark contrast in the XMCD images corresponds to a magnetization aligned along the x or z axis while bright contrast indicated an alignment along the $-x$ or $-z$ axis. Due to the sample alignment with respect to the X-ray propagation direction (z axis) the instrument is not sensitive to magnetization components along the y axis. The magnetic signal is expected to originate mainly from the M_x component because of the sample geometry.

A larger homogeneously magnetized sample in general will decay into domains of constant magnetization pointing into different directions to minimize its internal

energy. The equilibrium domain patterns for a large variety of structures and materials have been observed with static magnetic imaging techniques. Time-resolved approaches have also captured the dynamics followed by a weak transient perturbation of the equilibrium configuration [26–29]. However, observation of the essential process how (fast) an equilibrium domain pattern evolves out of a homogeneously magnetized sample was lacking so far. We have captured the destruction and recovery of the magnetization configuration in small $2 \times 2\,\mu m^2$ permalloy squares of 30 nm thickness. These elements will relax into a Landau pattern consisting of four triangular-shaped domains with a magnetization circling around a central vortex core (e.g. in Fig. 14.7 at a delay of 42.37 ns).

An intense current pulse launched into the coplanar waveguide on the sample can align the magnetization in such samples along the direction of the magnetic field that copropagates with the current pulse. By acquiring XMCD images using opposite photon helicities for several pump–probe delays, the destruction and recovery of the equilibrium Landau pattern can be monitored as a movie sequence with the time-resolved full-field X-ray microscope. Figure 14.7 shows the measured image sequence of the magnetization dynamics in two permalloy squares (I + II) located on the inner conductor of a CPW.

The indicated pump–probe delay is calibrated such that the peak amplitude of the magnetic field pulse of 438 ps FWHM duration is reached at 0 ps. The field of the excitation pulse is directed along the x axis. On arrival of the pulse the magnetization follows the excitation field and changes its direction on a fast timescale so that it points along the x axis (dark contrast) until a maximal alignment is reached at a delay of $\Delta t = 370$ ps with no detectable substructure. A closer look into the previous frames reveals that the vortex core in the center leaves the magnetic sample during destruction of the domain pattern (for a more elaborate discussion see [23]). Previous experiments have shown that the vortex core can be driven into an oscillatory motion by an external oscillating field and that it reverses its polarity at core velocities exceeding ≈ 300 m/s [30]. Due to the strong excitation field available here, we can study the vortex core motion in a new regime and find that the vortex core exceeds a velocity of 1 km/s and has no time to complete an oscillation period before it is ejected out of the sample.

After the pulse has vanished, the energetically unfavorable homogeneous magnetization configuration decays back into the equilibrium Landau pattern. The dynamics is similar for both squares (I + II) and up to 1 ns the M_x component (visible as dark contrast) is reduced homogeneously without any detectable substructure. A quantitative analysis of the gray values together with micromagnetic simulations [23] have shown that the majority of the magnetic polarization along the x axis is removed in this first fast phase when the x component decays from $M_x = 0.9 M_S$ down to $M_x = 0.3 M_S$ where M_S corresponds to the saturation magnetization. Subsequently, a zigzag domain starts building up on the top and another small M_x domain appears at the bottom until 3.37 ns where the decay of the polarization along the x axis slows down and reaches a value of $M_x = 0.2 M_S$ at 3 ns. Although the M_x polarization has almost vanished the dynamics still continues and during the next 10 ns the magnetization reorganizes into the final Landau state with an imbalanced domain size.
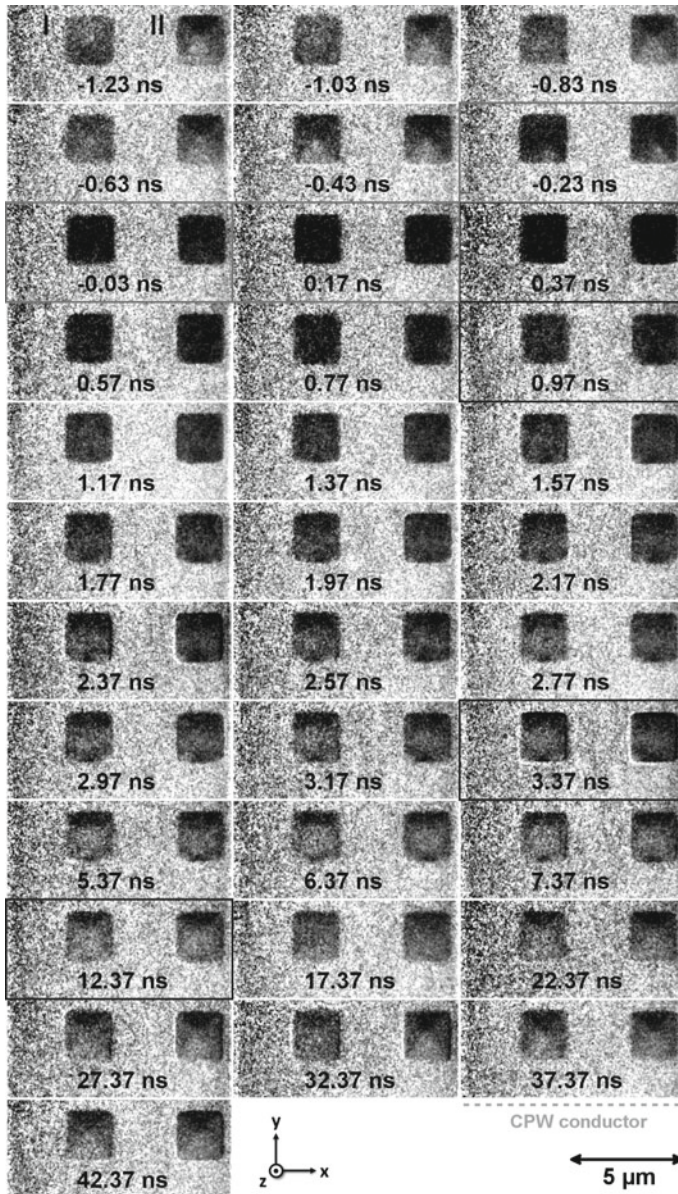
Fig. 14.7 Domain pattern destruction and recovery: Image sequence of the magnetization dynamics in two $2 \times 2\,\mu\text{m}^2$ permalloy squares (I + II) of 30 nm thickness exposed to a short magnetic field pulse (438 ps FWHM centered at 0 ps). Before arrival of the excitation pulse, the squares feature an equilibrium Landau domain pattern that consists of four domains. The pulse destroys this domain pattern and aligns the magnetization homogeneously along the x axis. After the pulse has vanishes the sample decays back to its Landau configuration. Adapted with permission from P. Wessels et al., Phys. Rev. B **90**, 184417 (2014) [23]. Copyrighted by the American Physical Society
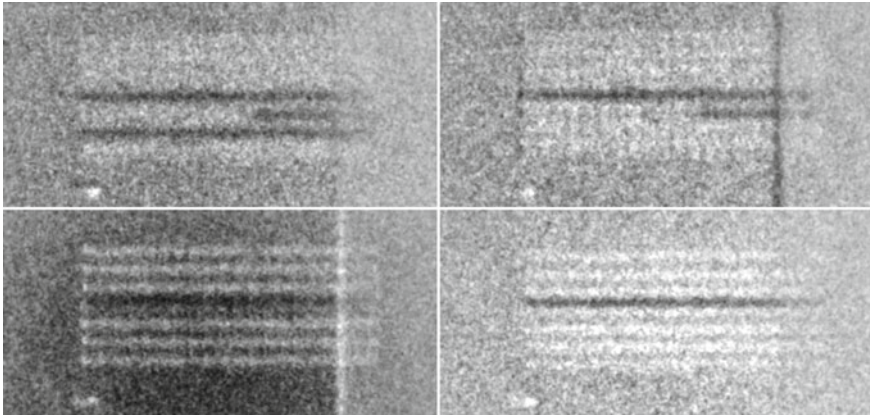
Fig. 14.8 Stochastic switching in a pump–probe / reset sequence: Dynamic magnetization of an array consisting of $400 \times 100\,nm^2$ elements separated by 50 nm horizontally and 250 nm vertically. The array partially overlaps with the waveguide conductor on the right and the XMCD images show the magnetization configuration at a fixed pump–probe delay Δt and constant reset pulse parameters after integrating the signal from several pump-probe cycles. The different magnetic orientation indicates a stochastic switching characteristic. Reproduced from P. Wessels, Ph.D. thesis (Verlag Dr. Hut, München, 2014) [1]

Between 12 ns and 42 ns the top M_x domain (black contrast) grows until the vortex core is positioned in the center of the square.

The previously discussed permalloy squares with a Landau magnetization pattern decay back into the ground state on their own. More complex magnetic systems such as arrays consisting of single domain particles coupled via their stray field can end up in a final stable state different from the initial state so that an active reset pulse is necessary to initialize the sample before the next measurement can begin (compare Fig. 14.1). Figure 14.8 shows XMCD images of an array of $400 \times 100\,nm^2$ elements separated by 50 nm horizontally and 250 nm vertically. For a pump–probe / reset cycle the magnetization of the whole array would be aligned along the $-x$ direction and then the elements on the waveguide switch their magnetization into the $+x$ direction. Due to coupling via the stray-field the chain reverses its magnetization direction element by element over time.

The images in Fig. 14.8 were taken by integrating the signal from several pump–probe cycles at the same delay and yet the dynamic magnetization configuration is different in all images indicating an unstable switching process so that a dynamic measurement was not possible since the pump–probe/reset approach relies on the reproducibility of the dynamics. In order to ensure a high reproducibility of the switching dynamics the indistinguishability of the elements and the spacings have to be improved. Moreover, external magnetic fields have to be compensated. Given a perfect sample preparation, simulations have shown that the switching dynamics should be observable with the instrument. Also arrays of lateral magnetic elements such as Co/Pt multilayer systems can be investigated and were imaged with the soft X-ray microscope [20].

14.3 Conclusion

In conclusion, two time-resolved instruments for imaging the dynamics of small magnetic structures have been set up. A laser based scanning Kerr microscope allows for the investigation of magnetic transport phenomena using visible light. An opto-electronic current source enables a direct observation of Damon-Eshbach as well as backward volume spin-wave packets with unusual dispersion relations so that the phase-fronts approach the excitation region while the wave packet propagate into the opposite direction. For experiments demanding a higher spatial resolution the first full-field transmission X-ray microscope has been set up that allows time-resolved measurements. The fundamental process of the destruction and recovery of equilibrium domain patterns out of uniform magnetization states can be followed with this instrument. Moreover, the vortex core motion in a strongly driven system has been studied where the core can not complete a round trip at its eigenfrequency and where the core velocity exceeds 300 m/s despite the fact that other experiments have observed a switching of the polarity at these velocities. First studies on non-reversible dynamics have been initiated.

References

1. P. Wessels, Time-resolved imaging of magnetic nanostructures in the visible and soft x-ray spectral range. Ph.D. thesis, University of Hamburg (2014)
2. S. Bonetti, R. Kukreja, Z. Chen, F. Macià, J.M. Hernàndez, A. Eklund, D. Backes, J. Frisch, J. Katine, G. Malm, S. Urazhdin, A.D. Kent, J. Stöhr, H. Ohldag, H.A. Dürr, Nat. Commun. **6**, 8889 (2015)
3. R. Frömter, F. Kloodt, S. Rößler, A. Frauen, P. Staeck, D.R. Cavicchia, L. Bocklage, V. Röbisch, E. Quandt, H.P. Oepen, Appl. Phys. Lett. **108**, 142401 (2016)
4. S.A. Wolf, D.D. Awschalom, R.A. Buhrman, J.M. Daughton, S. von Molnár, M.L. Roukes, A.Y. Chtchelkanova, D.M. Treger, Science **294**, 1488 (2001)
5. A.V. Chumak, V.I. Vasyuchka, A.A. Serga, B. Hillebrands, Nat. Phys. **11**, 453 (2015)
6. C. Chappert, A. Fert, F.N. Van Dau, Nat. Mater. **6**, 813 (2007)

7. M.P. Kostylev, A.A. Serga, T. Schneider, B. Leven, B. Hillebrands, Appl. Phys. Lett. **87**, 153501 (2005)
8. M. Jamali, J.H. Kwon, S.M. Seo, K.J. Lee, H. Yang, Sci. Rep. **3**, 3160 (2013)
9. K. Vogt, F.Y. Fradin, J.E. Pearson, T. Sebastian, S.D. Bader, B. Hillebrands, A. Hoffmann, H. Schultheiss, Nat. Commun. **5**, 3727 (2014)
10. P. Wessels, A. Vogel, J.N. Tödt, M. Wieland, G. Meier, M. Drescher, Sci. Rep. **6**, 22117 (2016)
11. H.J.J. Liu, G.A. Riley, K.S. Buchanan, IEEE. Magn. Lett. **6**, 4000304 (2015)
12. T. Satoh, Y. Terui, R. Moriya, B.A. Ivanov, K. Ando, E. Saitoh, T. Shimura, K. Kuroda, Nat. Photonics **6**, 662 (2012)
13. Z. Liu, F. Giesen, X. Zhu, R.D. Sydora, M.R. Freeman, Phys. Rev. Lett. **98**, 087201 (2007)
14. K. Perzlmaier, G. Woltersdorf, C.H. Back, Phys. Rev. B **77**, 054425 (2008)
15. V.E. Demidov, S.O. Demokritov, K. Rott, P. Krzysteczko, G. Reiss, Phys. Rev. B **77**, 064406 (2008)
16. V.E. Demidov, S. Urazhdin, S.O. Demokritov, Nat. Mater. **9**, 984 (2010)
17. M. Madami, S. Bonetti, G. Consolo, S. Tacchi, G. Carlotti, G. Gubbiotti, F.B. Mancoff, M.A. Yar, J. Akerman, Nat. Nanotechnol. **6**, 635 (2011)
18. P. Fischer, IEEE. Trans. Magn. **51**, 0800131 (2015)
19. S. Bonetti, J. Phys.: Condens. Matter **29**, 133004 (2017)
20. P. Wessels, M. Schlie, M. Wieland, J. Ewald, G. Abbati, S. Baumbach, J. Overbuschmann, T. Nisius, A. Vogel, A. Neumann, A. Meents, J. Viefhaus, H.P. Oepen, G. Meier, T. Wilhein, M. Drescher, J. Phys.: Conf. Ser. **463**, 012023 (2013)
21. P. Wessels, J. Ewald, M. Wieland, T. Nisius, G. Abbati, S. Baumbach, J. Overbuschmann, A. Vogel, A. Neumann, J. Viefhaus, H.P. Oepen, G. Meier, T. Wilhein, M. Drescher, J. Phys.: Conf. Ser. **499**, 012009 (2014)
22. J. Ewald, P. Wessels, M. Wieland, T. Nisius, A. Vogel, G. Abbati, S. Baumbach, J. Overbuschmann, J. Viefhaus, G. Meier, T. Wilhein, M. Drescher, AIP. Conf. Proc. **1696**, 020005 (2016)
23. P. Wessels, J. Ewald, M. Wieland, T. Nisius, A. Vogel, J. Viefhaus, G. Meier, T. Wilhein, M. Drescher, Phys. Rev. B **90**, 184417 (2014)
24. J. Viefhaus, F. Scholz, S. Deinert, L. Glaser, M. Ilchen, J. Seltmann, P. Walter, F. Siewert, Nucl. Instrum. Methods Phys. Res., Sect. A **710**, 151 (2013)
25. U. Vogt, M. Lindblom, P. Charalambous, B. Kaulich, T. Wilhein, Opt. Lett. **31**, 1465 (2006)
26. S.B. Choe, Y. Acremann, A. Scholl, A. Bauer, A. Doran, J. Stöhr, HA. Padmore. Science **304**, 420 (2004)
27. B. Van Waeyenberge, A. Puzic, H. Stoll, K.W. Chou, T. Tyliszczak, R. Hertel, M. Fähnle, H. Brückl, K. Rott, G. Reiss, I. Neudecker, D. Weiss, C.H. Back, G. Schütz, Nature **444**, 461 (2006)
28. A. Vogel, T. Kamionka, M. Martens, A. Drews, K.W. Chou, T. Tyliszczak, H. Stoll, B. Van Waeyenberge, G. Meier, Phys. Rev. Lett. **106**, 137201 (2011)
29. C. Behncke, M. Hänze, C.F. Adolff, M. Weigand, G. Meier, Phys. Rev. B **91**, 224417 (2015)
30. K.S. Lee, S.K. Kim, Y.S. Yu, Y.S. Choi, K.Y. Guslienko, H. Jung, P. Fischer, Phys. Rev. Lett. **101**, 267206 (2008)